Image-based computational homogenization and localization: comparison between X-FEM/levelset and voxel-based approaches

Wei-Dong Lian, Grégory Legrain, Patrice Cartraud

GeM Institute

GeM Institute UMR CNRS 6183
LUNAM Université
École Centrale de Nantes / Université de Nantes / CNRS,
1 Rue de la Noë, BP92101, 44321 Nantes, France.

Image-based computational homogenization and localization: comparison between X-FEM/levelset and voxel-based approaches

WD. Lian , G. Legrain , P. Cartraud

Preprint submitted to:
Computational Mechanics

Image-based computational homogenization and localization: comparison between X-FEM/levelset and voxel-based approaches

WD. Lian , G. Legrain , P. Cartraud

SUMMARY

In material science, images are increasingly used as input data for computational models. In most of the published papers, voxel-based finite element models are employed using a mesh that is automatically built by converting each voxel into a finite element. We have recently proposed (Legrain *et al.* , 2011) another computational approach for incorporating images in models, based on the extended finite element method (X-FEM) and levelsets. Its main advantages are that the mesh does not need to conform to the geometry and that a smooth representation of physical surfaces is obtained. The aim of this paper is to compare the two approaches in the framework of computational homogenization in elasticity, starting from material microstructural images. Attention will be paid to geometrical approximations, macroscopic properties and local quantities (e.g. stress oscillations, local error etc.). It is shown that the X-FEM/levelset approach is more efficient than voxel-based FEM. KEY WORDS: Image-based modeling , X-FEM , Levelset , Voxel-based mesh , Image Segmentation , Homogenization

Preprint submitted to: Computational Mechanics

1 Introduction

Recent advances in imaging techniques in materials science, see e.g. [32], have made it possible to capture two- and three-dimensional details of material internal structures at various length scales. A direct way of constructing the material geometry is possible by incorporating the data of a digital image into numerical models. This has been the crucial subject of numerous studies and projects, and image-based finite element models are now well recognized as a powerful mean of achieving this goal, see e.g. [43, 22]. Among them, voxel-based finite element models are the most popular [28]. The idea is to directly convert the labeled voxel information - a label is used to identify the different constituent materials of the image - into a geometrical model for a numerical analysis such as Finite Element Analysis (FEA). This so-called digital image-based FEM has been originally proposed in [21, 16] for bone and then used for the homogenization of composite materials, see e.g. [37]. With the help of image processing tools, each pixel or voxel could be identified as a finite element, and thus a voxel-based FE model is automatically generated. The voxel-based modeling usually includes the following three steps.

The first step consists in capturing, sampling and image preprocessing, which are assumed to have been done in this paper. For the second step, by means of various image segmentation methods such as edge detection, region growing, segmentation based on watersheds, levelset segmentation [17, 33], one could obtain a multi-labeled image where each voxel is assigned a label, chosen from a relatively small set of labels. The third step concerns the transformation of a multi-labeled image into a mesh file format compatible with FEM. Alternatively one could also make a programming interface in FEA program for automatically importing the multi-labeled image. It is worth emphasizing that image segmentation directly determines the quality of FE model, and thus is probably the most important step.

In spite of an easy and robust mesh generation, the voxel-based model leads to a huge computational cost, since the element size is the voxel size of the image. Moreover, the voxel-based model produces intrinsic jagged surfaces, within which high local stress oscillations exist [15]. Mesh refinement does not necessarily improve the local accuracy [41, 7]. Various voxel mesh smoothing algorithms [6, 4, 42] or post-processing filtration methods [15, 7] have been proposed to reduce local mean and maximum solution errors. However, considerable local oscillations were still observed along boundary elements, see [5].

In view of these limitations, we have recently proposed an alternative computational approach [22], based on the X-FEM [3, 11] and the levelset approach, for incorporating images into numerical models. One of the most appealing features of the X-FEM is that the mesh does not need to follow the geometrical boundaries, which clearly simplifies the complexity of mesh generation. The method is actually based on the partition of unity [26] and allows a representation of material interfaces through enrichment functions. Therefore, a regular mesh or structured mesh is sufficient for X-FEM modeling. Note that the regular or structured mesh can also be different from the regular grid of the image. Moreover the X-FEM can be coupled with the levelset approach. This coupling allows taking advantage of the segmentation capabilities of the levelset method. Thus, the location of the material interface is obtained naturally with the use of the levelset information (iso-zero curve or surface). As will be shown in the following, a key advantage of the levelset approach lies in the ability to obtain a smooth representation of physical surfaces.

Despite the voxel-based model has been used in numerous applications, it appears that less attention has been paid to the assessment of its accuracy [7, 1]. The objective of this work is thus to analyze the accuracy of the voxel-based FEM and X-FEM/levelset approach. The computational homogenization, along with the two approaches, is used to compute macroscopic mechanical properties of heterogeneous materials. Examples of fiber and particulate composite materials in elasticity are studied, their microstructure being characterized through a digital image. In this work, we also consider two realistic materials, a 2D ceramic-metallic composite material reported in [13] and a 3D foam material coming from food industry.

This article is organized as follows. In Section 2, the X-FEM and levelset approach are presented, consisting of the image segmentation and the X-FEM/Levelset coupling. Section 3 is dedicated to the computational homogenization procedure. In Section 4,

the proposed approach is verified through benchmark examples and compared to the voxel-based FEM. Finally, realistic examples are considered in Section 5 and concluding remarks are given.

2 Image-based computations with X-FEM and levelset approach

The approach presented here relies on two ingredients: (i) the levelset method [30, 33] and (ii) the eXtended Finite Element Method [2, 35, 3]. The levelset method is the core of the approach, as it is used for each stage of the process: first during the segmentation process, then as a mean to embed the geometrical information into the X-FEM, and finally to define the enrichment functions that are used to enhance the approximation. The levelset representation of a curve Γ (in 2D) or a surface (in 3D) is described by the iso-zero contour (in 2D) or surface (in 3D) of an implicit scalar function $\Phi(\boldsymbol{x})$:

$$\Gamma = \{\boldsymbol{x} \,|\Phi(\boldsymbol{x}) = 0\} \tag{1}$$

This function is called levelset function and is usually chosen as the signed distance to the curve (resp. surface). The shape of the curve (resp. surface) Γ can be modified based on the evolution of $\Phi(\boldsymbol{x})$, following a transport equation. With respect to explicit representation of the interfaces, the levelset approach handles naturally topological changes such as merging or splitting of Γ.

2.1 Levelset image segmentation

The levelset method has been used with success in the context of image processing [33, 40]. In the case of image segmentation, the main advantage is that arbitrary shapes can be modeled and topological changes (e.g. merging and splitting) are handled implicitly. In levelset based segmentation, images features such as intensity, gradient or edges are used to propagate an initial guess and lock its iso-zero on the boundaries of the objects to be segmented. The propagation is based on the following PDE [17]:

$$\frac{\mathrm{d}\Phi}{\mathrm{d}t} = -\alpha \boldsymbol{A}(\boldsymbol{x}) \cdot \nabla\Phi - \beta P(\boldsymbol{x})\big|\nabla\Phi\big| + \gamma Z(\boldsymbol{x})\kappa\big|\nabla\Phi\big| \tag{2}$$

where $\Phi(\boldsymbol{x}, t)$ is the levelset function, scalar P adjusts outward motion (propagation term), Z scales the motion by mean curvature κ of the front, and the advection term $\boldsymbol{A}$ represents a rigid body motion. In this equation, parameters $\boldsymbol{A}(\boldsymbol{x})$, $P(\boldsymbol{x})$ and $Z(\boldsymbol{x})$ are function of the intensity values of the image. The scalar constants α, β and γ control the relative influence weight of each of the terms, and depend on the segmentation scheme[1]. In this work, the so-called *threshold levelset image segmentation* scheme is employed

[1] For instance, *Shape Detection Segmentation* scheme (see [17]) considers the curvature term to smooth the areas with high curvature. Weights β and γ control the trade-off between the expansion and the smoothing. One may adapt these weights according to the last segmentation result until a reasonable result is obtained.

where the advection term $\boldsymbol{A}(x)$ is not used (i.e. $\alpha = 0$) and $\beta = \gamma = 1$ is set to balance the influence of the propagation term and curvature term (surface smoothing). The propagation term $P(\boldsymbol{x})$ directly depends on the grayscale intensity of the image

$$P(\boldsymbol{x}) \quad = \quad \begin{cases} g(\boldsymbol{x}) - L & g(\boldsymbol{x}) < \frac{1}{2}(U-L) + L \\ U - g(\boldsymbol{x}) & otherwise \end{cases} \tag{3}$$

where $g(\boldsymbol{x})$ represents the intensity of the input image, U and L denote the range of the gray levels. This range identifies the material phase of interest and has to be declared by the user. Note that here global threshold is used, but a locally adapted threshold is also possible if lightness conditions vary over the image. Albeit being crude, this segmentation scheme requires little or no image preprocessing. However, an initial guess $\Phi(\boldsymbol{x}, t = 0)$ is required to be provided as an user input. Then, this initial levelset is evolved by solving Eq. (2) until stationarity is achieved (with respect to a stagnation criteria). The shape of this initialization conveys a strong influence on segmentation time, which also depends on the surface area of the volume and the distance the front has to propagate. The closest the initial guess to the segmented object, the faster the process. In the following, a regular layout of spheres will be considered as an initial guess, see Fig. 1. The radius of the spheres and their corresponding intervals depend on the details to be captured for a specific microstructure.

Fig. 2 illustrates the procedure of levelset image segmentation. With time passed on, some regions of the initial levelsets will propagate, and the others will shrink simultaneously according to Eq. (3). Finally one obtains the segmented objects.

The iso-zero of the levelset that is obtained as an output in the final step, is calculated to subpixel precision [17] through the interpolation of the field between pixels. Then the segmented geometry can be located inside the pixels. The output *levelset image* where each voxel value (float type) corresponds to the levelset value[2], appears as an input geometry for X-FEM (see Section 2.2). Meantime, one can also extract *multi-labeled images* from the *levelset image* using *binary threshold image filter*.

2.2 The eXtended Finite Element Method & Levelset coupling

The extended finite element method (X-FEM) [11] is an extension of the finite element method that was developed in order to overcome some limitations of the finite elements. The main objective was to improve it when dealing with complex geometries, in order to specify the field approximations independently from the geometries. From the original contribution focused on fracture mechanics [2], the method has evolved and has been applied, in particular to the treatment of problems involving material discontinuities such as holes [36], or material interfaces for mechanical applications [29, 8] and thermal applications [44]. The approximation is enhanced by means of enrichment functions that are tailored to a particular problem. This is achieved by using the partition of

[2]I.e. the levelset value at the center of each voxel: positive indicates one phase, negative denotes another phase.

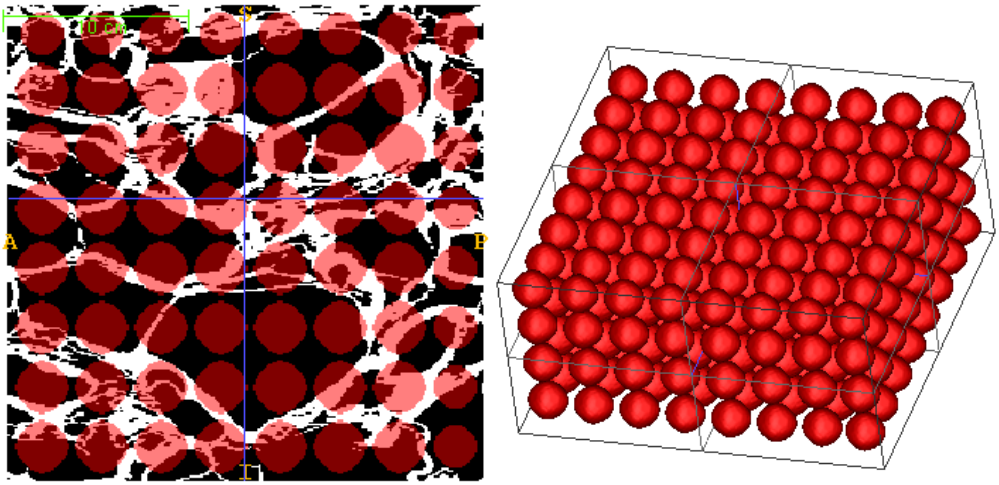

Figure 1: 2D and 3D user initialized level sets. The regular layout of solid circles in the left figure stands for the initial levelset of 2D image. The right figure depicts the initial levelset for 3D image, which can be used for the 3D foam material in Section 5.3.

unity technique proposed in [26]. The X-FEM approximation of a field $U(\boldsymbol{x})$ takes the following form:

$$U^{\text{X-FEM}}(\boldsymbol{x}) = \underbrace{\sum_{i \in I} u_i N_i(\boldsymbol{x})}_{\text{Classical}} + \underbrace{\sum_{j \in J} a_j N_j(\boldsymbol{x}) F(\boldsymbol{x})}_{\text{Enriched}} \tag{4}$$

where u_i stands for the classical degrees of freedom (dofs), N_i denotes the finite element shape function associated to dof i, $F(\boldsymbol{x})$ is the enrichment function and a_j stands for the enriched dofs associated to shape function N_j and enrichment function $F(\boldsymbol{x})$. The set I (resp. J) represents the nodes (resp. enriched nodes) of the mesh. In this form, only one enrichment function was considered, but an arbitrary number could be added. In practice, the set of enriched dofs J remain small, as only the shape functions whose support is cut by the interface are enriched (see Fig. 3a for the case of an elliptic inclusion in a square domain).

In Eq. (4), the *Classical* term indicates classical finite element approximation, whereas the *Enriched* one represents the enriched part of the approximation that enables to model discontinuities independently of the underlying finite element mesh. The choice of $F(\boldsymbol{x})$ is crucial in order to improve the finite element approximation. In the case of material interfaces, a strain discontinuity has to be represented across the interface: the enrichment function must be continuous while its derivative is discontinuous. An initial proposition was presented in [36] considering the absolute value of the levelset as an enrichment:

$$F(\boldsymbol{x}) = |\Phi(\boldsymbol{x})| \tag{5}$$

An optimal convergence rate could not be achieved with this enrichment (see [29]). The

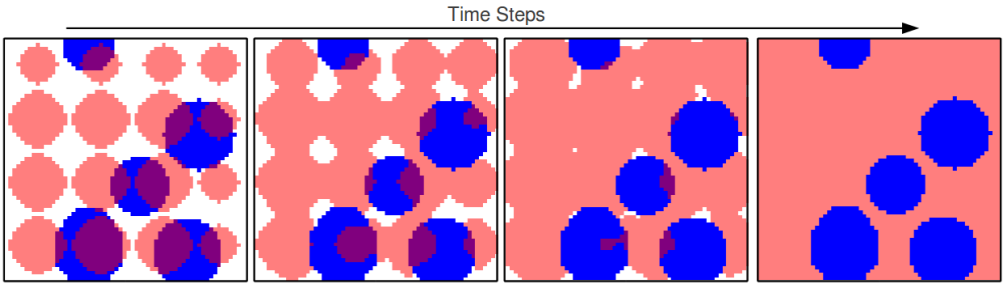

Figure 2: Levelset image segmentation working procedure. In the first image from left, the blue regions stand for the segmented objects and the regular spinel-red circles are initial levelset. From the second to the fourth image, the initial levelset propagates for the part outside the segmented objects, and shrink for the inside part.

so-called *ridge function* [29] is thus employed in this work to obtain an optimal rate of convergence:

$$F(\boldsymbol{x}) = \sum_i N_i(\boldsymbol{x}) \left|\Phi_i\right| - \left|\sum_i N_i(\boldsymbol{x})\Phi_i\right| \tag{6}$$

where Φ_i indicates nodal levelset values. The enrichment function $F(\boldsymbol{x})$ is shown in Fig. 3b, meeting the desired requirement of strain discontinuity across the interface. Note that this enrichment function has been used in [45] for computing effective properties of nanocomposites. In the remaining of this paper, only simplex meshes will be considered for the computations (triangles in 2D, tetrahedra in 3D). In addition, both mechanical approximation and levelset interpolation will be restricted to linear Lagrange polynomials.

The geometrical information is embedded into the model through the levelset function $\Phi(\boldsymbol{x})$ that is the output of the segmentation process. This levelset is defined at the center of each pixel of the original image, as mentioned in Section 2.1. The pixel-based levelset is then projected onto the computational mesh, and thus leading to geometrical approximations, even if the element size is similar to the size of one pixel. Different strategies are discussed in the following section in order to optimize the geometrical accuracy. Finally, an illustration of the proposed work-flow is presented in Fig. 4.

2.3 Meshing strategies

The density of computational mesh directly affects the accuracy of the X-FEM solution, as the levelset is interpolated on the computational mesh after projection. Despite X-FEM allows the use of uniform meshes, the mesh should be fine enough to represent the geometrical information. Notice that the mesh density only affects the accuracy near the material interface. Therefore, an octree-based meshing strategy using quadtree data structure [10], was proposed to keep maximal geometrical accuracy near the material interface [22]. The highest level of quadtree usually corresponds to the pixel size, i.e. only the smallest elements are governed by the pixel size. This meshing process can be

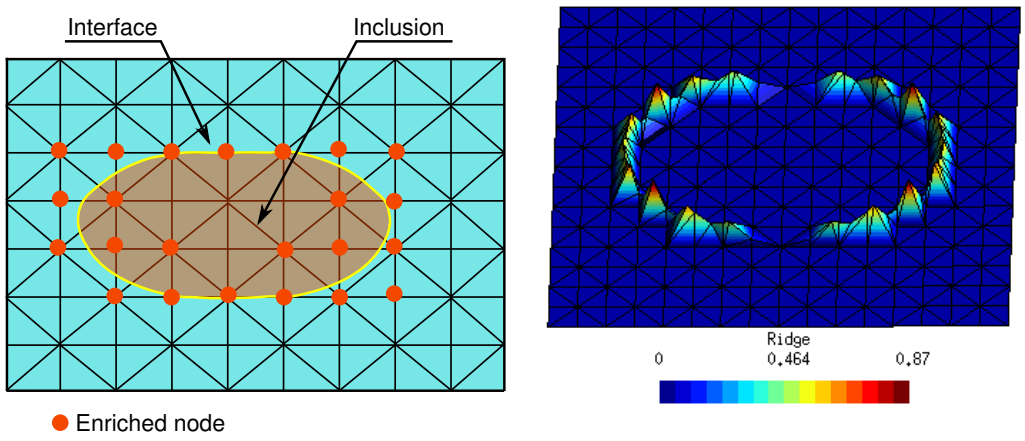

(a) (b)

Figure 3: (a) The X-FEM enrichment of the material interface (b) The ridge function for the case of a square plate with an elliptical inclusion in its center

viewed as a non-uniform coarsening procedure of the pixel-based mesh. For a maximal accuracy, pixel-sized elements are considered near the interfaces (full resolution), whereas it can be coarsened in less critical regions, i.e. as one moves away from the material interface. Meanwhile, the coarsening process can also be conducted using an initial grid that is coarser than the original image (group of $n \times n$ pixels). Note that no projection is involved during the coarsening process, thus ensuring the computational efficiency. The applications of 2D and 3D Octree meshes and their accuracy will be discussed in Section 5.2 and Section 5.3.

3 Homogenization problems

In order to compute effective properties of heterogeneous materials, the first-order computational homogenization consistent with Hill-Mandel principle is used in this work, see [27, 18, 19]. In general, the computational homogenization consists in solving a boundary value problem on a RVE (representative volume element). The determination of the RVE size is not addressed in this paper. However, the stochastic homogenization approaches allow the *a posteriori* definition of the physical RVE size with the help of a statistical analysis, see [19, 12] for more details. At the macroscopic scale, the volume average stress and strain over the RVE V are denoted by $\boldsymbol{\Sigma}$ and $\boldsymbol{E}$ respectively

$$\begin{cases} \boldsymbol{\Sigma} = \langle \boldsymbol{\sigma} \rangle = \frac{1}{|\Omega|} \int_\Omega \boldsymbol{\sigma} d\Omega \\ \boldsymbol{E} = \langle \boldsymbol{\varepsilon} \rangle = \frac{1}{|\Omega|} \int_\Omega \boldsymbol{\varepsilon} d\Omega \end{cases}$$

where $\boldsymbol{\sigma}$ and $\boldsymbol{\varepsilon}$ stands for microscopic stress and strain. The homogenized behavior relates $\boldsymbol{\Sigma}$ to $\boldsymbol{E}$ and is found from the solution of a localization problem. In this paper

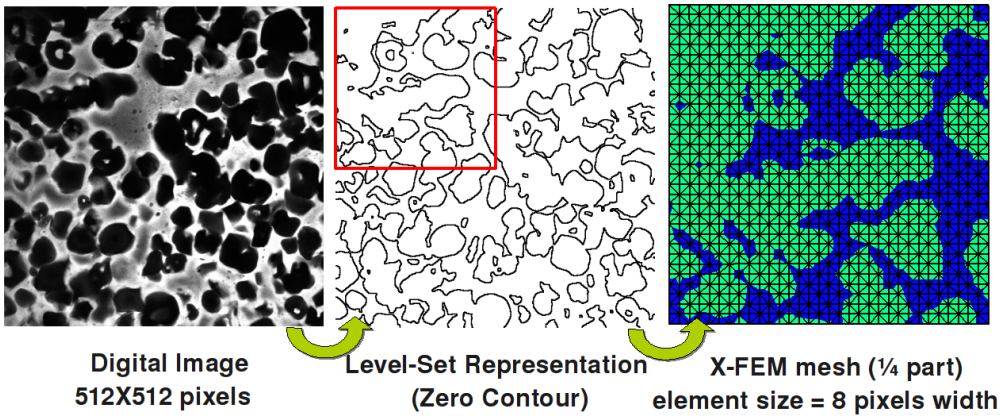

Figure 4: X-FEM/levelset modeling procedure where the colors in X-FEM mesh stand for different phases captured with zero-levelset. Despite the element size of X-FEM mesh is equal to the size of 8 pixels, the material interfaces are clearly located within elements.

the case of elasticity is studied, and thus the localization problem is an elastic problem posed on the RVE V, with data which can be $\boldsymbol{\Sigma}$ or $\boldsymbol{E}$, such that:

$$\begin{cases} \text{div}\boldsymbol{\sigma} = 0 & \text{on } V \\ \boldsymbol{\sigma} = \boldsymbol{c} : \boldsymbol{\varepsilon}, & \boldsymbol{\varepsilon} = \frac{1}{2}\left[\nabla \boldsymbol{u} + (\nabla \boldsymbol{u})^T\right] \end{cases} \tag{7}$$

with boundary conditions defined with given macroscopic data $\boldsymbol{\Sigma}$ or $\boldsymbol{E}$. Classically three types of boundary conditions are available:

- Kinematic uniform boundary conditions (KUBC):

$$\boldsymbol{u}(\boldsymbol{x}) = \boldsymbol{E} \cdot \boldsymbol{x} \quad \forall \boldsymbol{x} \in \partial V \tag{8}$$

  where $\boldsymbol{u}(\boldsymbol{x})$ is the imposed displacement field at point $\boldsymbol{x}$ of the boundary ∂V.

- Static uniform boundary conditions (SUBC):

$$\boldsymbol{t}(\boldsymbol{x}) = \boldsymbol{\Sigma} \cdot \boldsymbol{n}(\boldsymbol{x}) \quad \forall \boldsymbol{x} \in \partial V \tag{9}$$

  where $\boldsymbol{t}(\boldsymbol{x})$ and $\boldsymbol{n}(\boldsymbol{x})$ denote respectively the traction vector and the normal vector at point $\boldsymbol{x}$ of the boundary ∂V.

- Periodicity conditions (PERIODIC):

$$\boldsymbol{u}(\boldsymbol{x}) = \boldsymbol{E} \cdot \boldsymbol{x} + \boldsymbol{u}^*(\boldsymbol{x}) \quad \forall \boldsymbol{x} \in V \tag{10}$$

  where the fluctuation $\boldsymbol{u}^*(\boldsymbol{x})$ is periodic. It takes the same values on the opposite faces of V and the traction vector $\boldsymbol{\sigma}(\boldsymbol{x}) \cdot \boldsymbol{n}(\boldsymbol{x})$ takes opposite values.

Once the localization problem Eq. (7) with a set of boundary conditions is solved, the homogenization behavior is defined as

$$\boldsymbol{\Sigma} = \boldsymbol{c}^{\text{hom}} : \boldsymbol{E} \tag{11}$$

In the case of linear elasticity, the apparent stiffness tensor can be obtained by solving 6 independent loadings in 3D, corresponding to a unit $\boldsymbol{E}$ (for KUBC and PERIODIC) or $\boldsymbol{\Sigma}$ (for SUBC). In general, for periodic microstructures, PERIODIC is naturally preferred. In case of non-periodic microstructures, PERIODIC could still be applied, since it is the most efficient in terms of convergence rate for determining the size of the RVE, see e.g. [19, 20].

4 Validation examples

4.1 Model assessment via effective properties

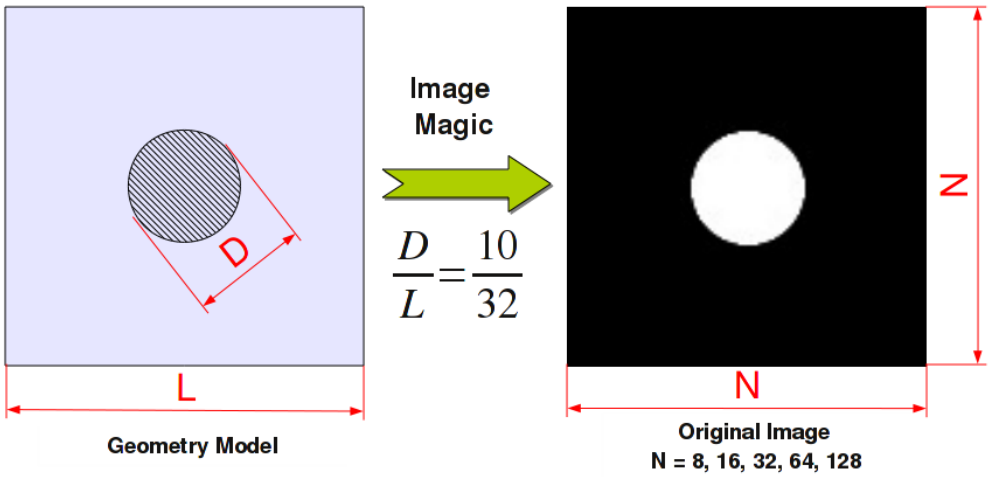

Figure 5: Cell geometry of a one fiber model

The RVE geometry of the first example is shown in Fig. 5. A square RVE with a circular inclusion is considered. From this geometry five images with different image resolutions ($N = 8, 16, 32, 64, 128$), are generated from ImageMagic [34] considering $\frac{D}{L} = \frac{10}{32}$ as input parameter. For each image, the corresponding *levelset image* (input geometry for X-FEM, in Fig. 7b) and the corresponding *multi-labeled image* (input geometry for voxel-based FEM, in Fig. 7a) are produced through the same image segmentation procedure as mentioned in Section 2.1. Then for each image, a mesh is built with an element size $h = \frac{128}{N}$. The modeling procedure is shown in Fig. 6. Note that besides the pixel-based and X-FEM meshes, a conforming mesh is also considered. In the following the solution obtained from this conforming mesh is referred to as the reference solution.

Volume fraction is first used to assess the geometrical error. The evolution of volume fraction as a function of mesh size is depicted in Fig. 8. It is clear that the levelset

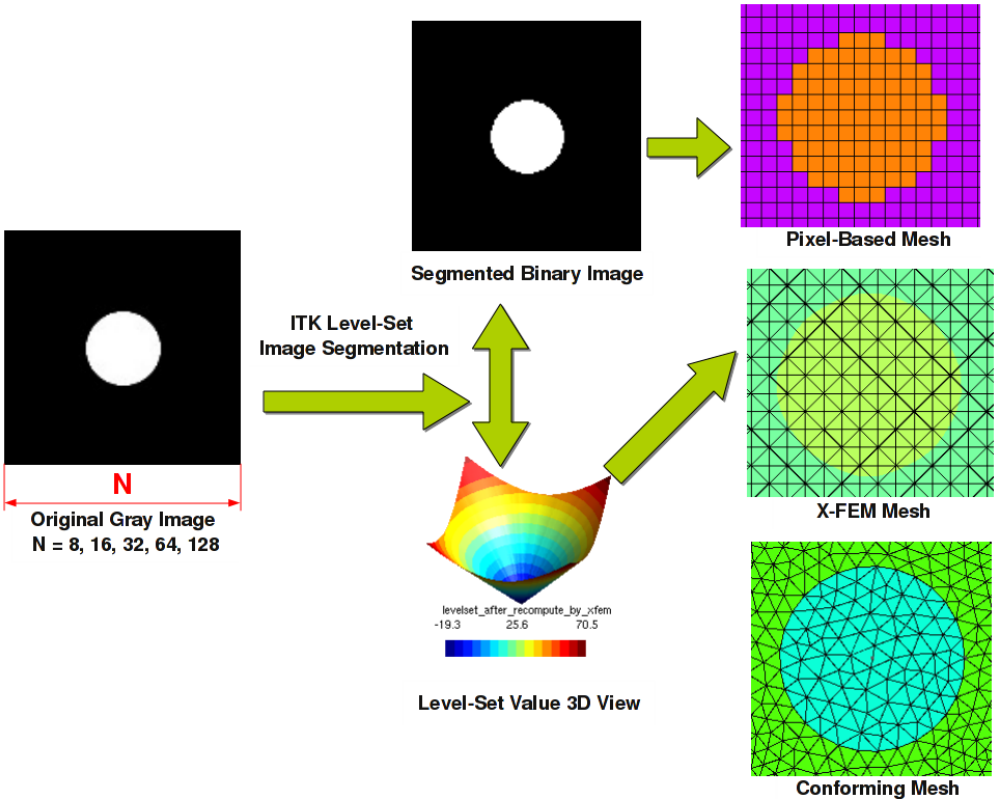

Figure 6: Voxel-based FEM and X-FEM modeling procedure

geometry for the X-FEM model is more smooth than that for voxel-based FEM, since levelset leads to a piece-wise linear representation of geometrical interface. In addition, from the image $N = 32$, the volume fraction for X-FEM is very close to the reference one ($V_f^{fiber} = 7.67\%$) while the voxel-based volume fraction converges very slowly. X-FEM coupling levelset is less sensitive to image resolution (mesh size) than voxel-based FEM. For a fixed accuracy, X-FEM could employ a coarser mesh than voxel-based FEM to decrease the computational cost.

Homogenization computations using X-FEM and voxel-based FEM are conducted here to study under plain strain assumption the influence of the image resolution on apparent bulk and shear moduli. In the parametric study, Poisson's ratio of the two phases (matrix, inclusion) is $\nu_i = \nu_m = 0.3$, and the Young's modulus for the matrix is ($E_m = 1$ GPa). In order to study different contrasts between the fiber and the matrix, the Young modulus of the inclusion is $E_i = \{0.001, 0.1, 10, 1000\}$ GPa. Periodic boundary conditions are used here and apparent properties (bulk and shear moduli) are calculated using the approach presented in [18].

The numerical results are given in Fig. 9 and Fig. 10 where conforming FEM solution with the finest mesh is considered as the reference solution. The X-FEM results are very close to the conforming FEM results (the difference is less than 1%) for different

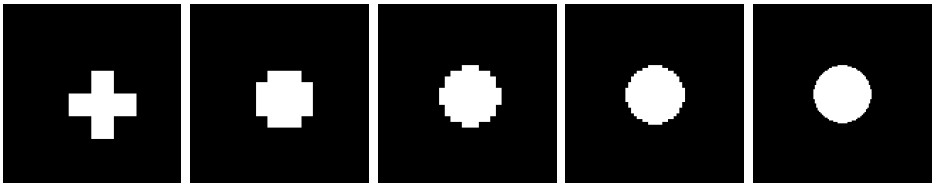

(a) Multi-labeled Images: 8X8 16X16 32X32 64X64 128X128 (from left to right)

(b) Levelset Views: 8X8 16X16 32X32 64X64 128X128 (from left to right)

Figure 7: Voxel-based geometry and X-FEM geometry

mesh sizes. By contrast, a significant difference between pixel-based and conforming FEM results is observed. Obviously the main part of this difference comes from the geometrical error. As can be seen from Fig. 8, using a pixel-based mesh leads to an overestimation of the volume fraction of the inclusion. Consequently, an overestimation of the macroscopic properties is observed in the case where the inclusion is stiffer than the matrix (see Fig. 10). The reverse is found when the matrix is stiffer (see Fig. 9). Thus, comparing to reference results, the X-FEM results are acceptable for the mesh size $h \leq 4$ (corresponding to $N = 32$) whereas even with $N = 128$, the pixel-based results are less accurate.

4.2 Model assessment via analysis of local quantities

To investigate the accuracy of X-FEM and voxel-based FEM at the microscopic scale, a bi-material boundary value reference problem with analytical solution is considered. This problem, shown in Fig. 11, is treated with the plane strain assumption. The material constants in Ω_1 and Ω_2 are chosen as $E_1 = 1\,\text{GPa}$; $\nu_1 = 0.25$ and $E_2 = 10\,\text{GPa}$; $\nu_2 = 0.3$ respectively. The boundary conditions are imposed as $u_1 = 10^{-3}x_1$, $u_2 = 10^{-3}x_2$ on the boundary Γ_2. The exact radial (u_r), hoop (u_θ) displacements, radial (ε_{rr}), hoop ($\varepsilon_{\theta\theta}$) strains, radial ($\sigma_{rr}$) and hoop ($\sigma_{\theta\theta}$) stresses are available in [36].

For the sake of simplicity, we extract a square domain ($W = H = 2$, $a = 0.4$, $b = 2.0$) from the model in Fig. 11 as a computational model. The exact tractions deduced using the exact σ_{rr} and σ_{tt}, are imposed on the boundary of this domain. Meanwhile, appropriate displacement constrains are considered to avoid rigid body motions. In order to study the accuracy of X-FEM and voxel-based FEM, a convergence study is conducted using uniform mesh with element size $h = W/2^n$ ($n = 3$, 4, 5, 6, 7, 8 respectively). The

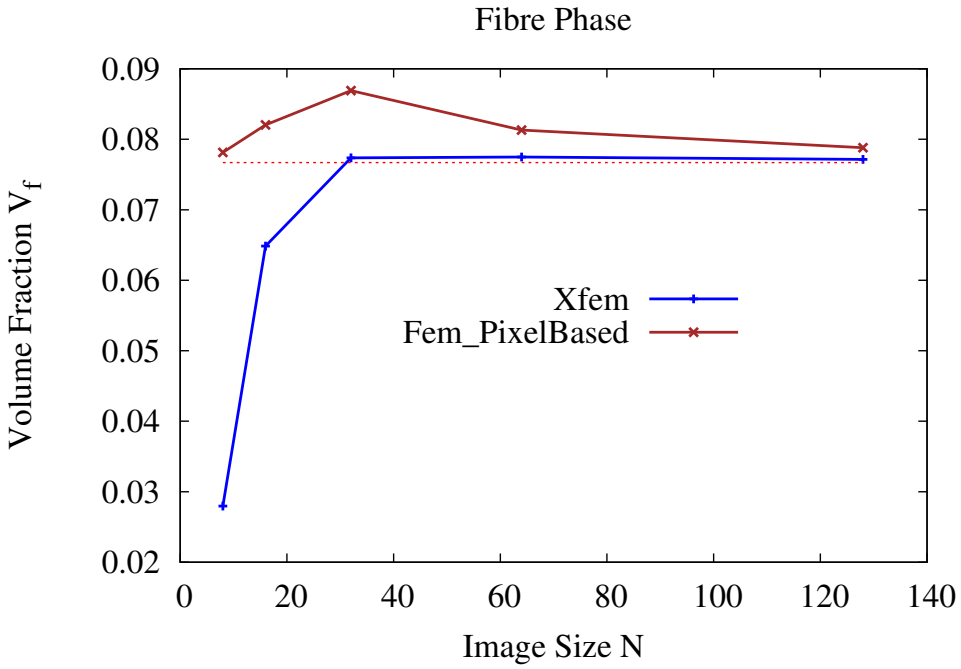

Figure 8: Volume fraction of fibres as a function of image resolution N

error is defined using the energy norm, formulated as:

$$\epsilon_{\text{rela}}^{\text{norm}} = \frac{\sqrt{\int_\Omega \boldsymbol{\varepsilon}(\boldsymbol{u}^h - \boldsymbol{u}^{ex}) : \boldsymbol{c} : \boldsymbol{\varepsilon}(\boldsymbol{u}^h - \boldsymbol{u}^{ex}) \mathrm{d}\Omega}}{\sqrt{\int_\Omega \boldsymbol{\varepsilon}(\boldsymbol{u}^{ex}) : \boldsymbol{c} : \boldsymbol{\varepsilon}(\boldsymbol{u}^{ex}) \mathrm{d}\Omega}} \tag{12}$$

where u^h is FE approximation solution and u^{ex} is the exact solution.

Fig. 12 shows the evolution of this global error as a function of the mesh size. It can be seen that the X-FEM convergence rate ($alpha$=0.9065 indicates the rate of convergence with respect to the average element size) nearly reaches the *optimal* finite element convergence ($alpha$=1). This result is consistent with the convergence rate reported in [29] where it was noticed that the accuracy of X-FEM with a non-conforming mesh was very close to a conforming FEM. Meanwhile, voxel-based FEM exhibits a fairly poor convergence rate ($alpha$=0.5548). Although the error norm defined in Eq. (12) is a global norm, the main contribution to this error norm is produced by the elements near the material interface. The exact error contributions with mesh $n = 6$ depicted in Fig. 13, indicates the distribution of the local error. From this comparison, it is evident that X-FEM benefits a very smaller local error than voxel-based FEM near material interface.

Another way to assess the models accuracy consists in comparing local stress results to the analytical solution. This is performed first for Von-Mises stress. At the material interface, this stress is discontinuous: there is a jump from the value of 2.15 MPa in

Ω_1, to 23.9 MPa in Ω_2, thus the comparison should not be conducted just here (i.e. $r = a$). Instead it is made in the domain Ω_2 near the material interface (i.e. $r = 1.04a$ and $\theta \in [0, \frac{\pi}{2}]$). The results are presented in Fig. 14 for two mesh densities. Note that constant stress state is obtained within each triangle element as a linear interpolation is used. For the coarsest one (n=4), due to the jagged interface of the voxel-based model, some parts of the model at $r = 1.04a$ belong to Ω_1, which explains the value of 2.15 MPa obtained at some points. Generally the geometrical error decreases as the mesh is refined as shown in Fig. 14b for the cases of X-FEM and conforming FEM. However, in Fig. 14b for the voxel-based model, significant oscillations are still observed, which has also been reported in [5, 15]. In addition, for voxel-based models, the region of significant influence of jagged interfaces may vary for different mesh densities (i.e different topologies). This explains why the fluctuation for voxel-based models is maximal near $\theta = 0$ and $\theta = 90$ for $n = 7$ in Fig. 14b, but around $\theta = 30$ and $\theta = 60$ for $n = 4$ in Fig. 14a. Thus the mesh refinement of the voxel-based model will not necessarily improve the local accuracy as reported in [41]. Despite oscillations also exist for X-FEM and conforming FEM models, they appear to be small versus voxel-based models and their accuracy is improved with mesh refinement.

To evaluate the local accuracy a step further, the distribution of σ_{11} is also compared in Fig. 15 where the element size is $h = W/2^7$ (i.e. $n = 7$). For comparison purpose, the same configuration[3] of contour plot of stress distribution is employed for the four cases in Fig. 15. Consequently, the finite elements with stress values out of the exact min-max range around the material interfaces will be hidden. Clearly, more element are hidden for the case of voxel-based FEM, but not for the X-FEM and conforming FEM. The resulting stress distributions for X-FEM and conforming FEM are quite similar. Meanwhile, voxel-based FEM exhibits fairly worst stress distribution along the material interface, overestimated on one side and underestimated on the other side. The minimum and maximum of σ_{11} for different mesh densities are also given in Tab. 1. It implies that the X-FEM and conforming FEM do converge to the exact minimum and maximum stresses (min=4.3088, max=31.4394, in MPa) for mesh refinement, but not the voxel-based FEM.

In summary, this example shows that the validation of voxel-based model must be assessed through careful considerations with regard to local quantities. Nevertheless, the voxel-based FEM might still be employed if quantities of interest are macroscopic physical properties.

5 Numerical examples

In this section, three different 2D and 3D RVE geometries are considered: (i) matrix-fiber composite with randomly distributed fibers which is numerically generated; (ii) 2D stellite and (iii) 3D foam materials. Among them, the first example is conducted with a randomly generated geometry, while the two last examples involve real materials. Note however that in all these examples, the starting point of the geometry is an image. These

[3]Number of contour lines, minimum and maximum values.

exact solution: min=4.3088; max=31.4394						
element size	Conforming FEM		X-FEM		voxel-based FEM	
$h = W/2^n$	min	max	min	max	min	max
n=3	3.83	34.9	3.31	40	3.45	24.5
n=4	3.90	33.7	2.79	33.7	1.98	32.9
n=5	3.90	33.2	3.83	32.1	1.51	35.7
n=6	3.98	32.6	3.96	32.3	2.09	37.3
n=7	4.17	32.1	4.09	31.9	1.26	39.9
n=8	4.21	31.7	4.21	31.6	1.28	42.9

Table 1: Minimum and maximum σ_{11} (MPa) for different approaches

examples have been solved using X-FEM and corresponding results have been presented In [22]. In the present paper, besides X-FEM, voxel-based FEM and conforming FEM are used. In each case, the comparison between X-FEM and voxel-based FEM is conducted, taking conforming FEM solutions as the reference ones. Besides accuracy, the computational cost of XFEM/levelset and the voxel-based FEM will also be investigated in the following.

5.1 Random fiber composite

The elastic as well as inelastic response of composite material is strongly influenced by its microstructure. Many random models characterizing the micro-morphology of real materials based on the statistical description are available. In this work, a randomly-distributed fiber image is generated using the random field approach (see [31]) in order to compare apparent properties computed from different approaches.

5.1.1 Numerical results

The random model image ($W = H = 512$ pixels) depicted in Fig. 16a is considered using X-FEM, voxel-based FEM and conforming FEM (element size $h = W/2^n$, $n = 6, 7, 8, 9$). The solution of conforming FEM with $n = 9$ is referred to as the reference solution. Fibers are assumed to be unidirectional with volume fraction 28.3%. The Poisson's ratios are both fixed to $\nu_i = \nu_m = 0.3$ and the Young's moduli are taken as $E_i = \{0.001, 0.1, 10, 1000\}$ and $E_m = 1$ respectively. KUBC are imposed, since the geometry is not periodic. The aim here is to compare apparent properties provided by the three numerical models for a given homogenization approach, rather than to discuss the choice of the best homogenization approach in terms of accuracy of apparent properties. These apparent elastic properties are obtained as a function of mesh size and are reported in Fig. 17 and Fig. 18. For macroscopic properties, it is shown that the bulk and shear moduli computed from X-FEM are similar to those obtained from conforming FEM. The small oscillations that appear in the shear modulus when $E_i/E_m = 10.$ are linked to the fact that the volumic fraction of the inclusions do not converge monotonously to

its limit value. For instance, coarser mesh cannot represent accurately the geometry as mesh size is close to the dimension of the inclusions (2.5 elements across the diameter in the case of the coarser one). This uncertainty on the geometry is propagated to the volumic fraction, and thus to the mechanical behavior. The conclusion here is thus the same as the one-fiber case discussed in Section 4.1.

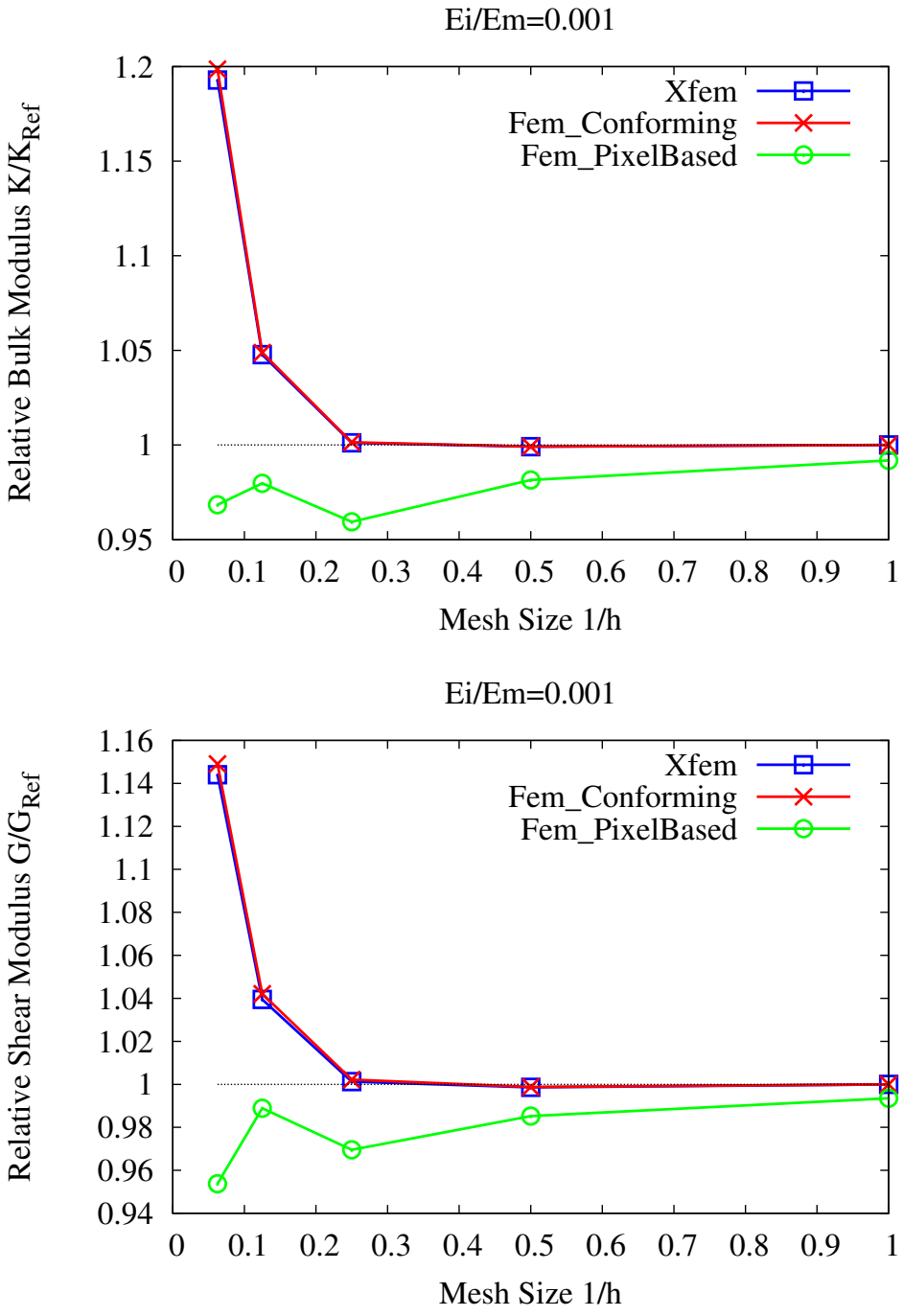

Figure 9: Comparison between voxel-based FEM and X-FEM for macroscopic properties as a function of mesh size h on the contrast $E_i/E_m = 0.001$

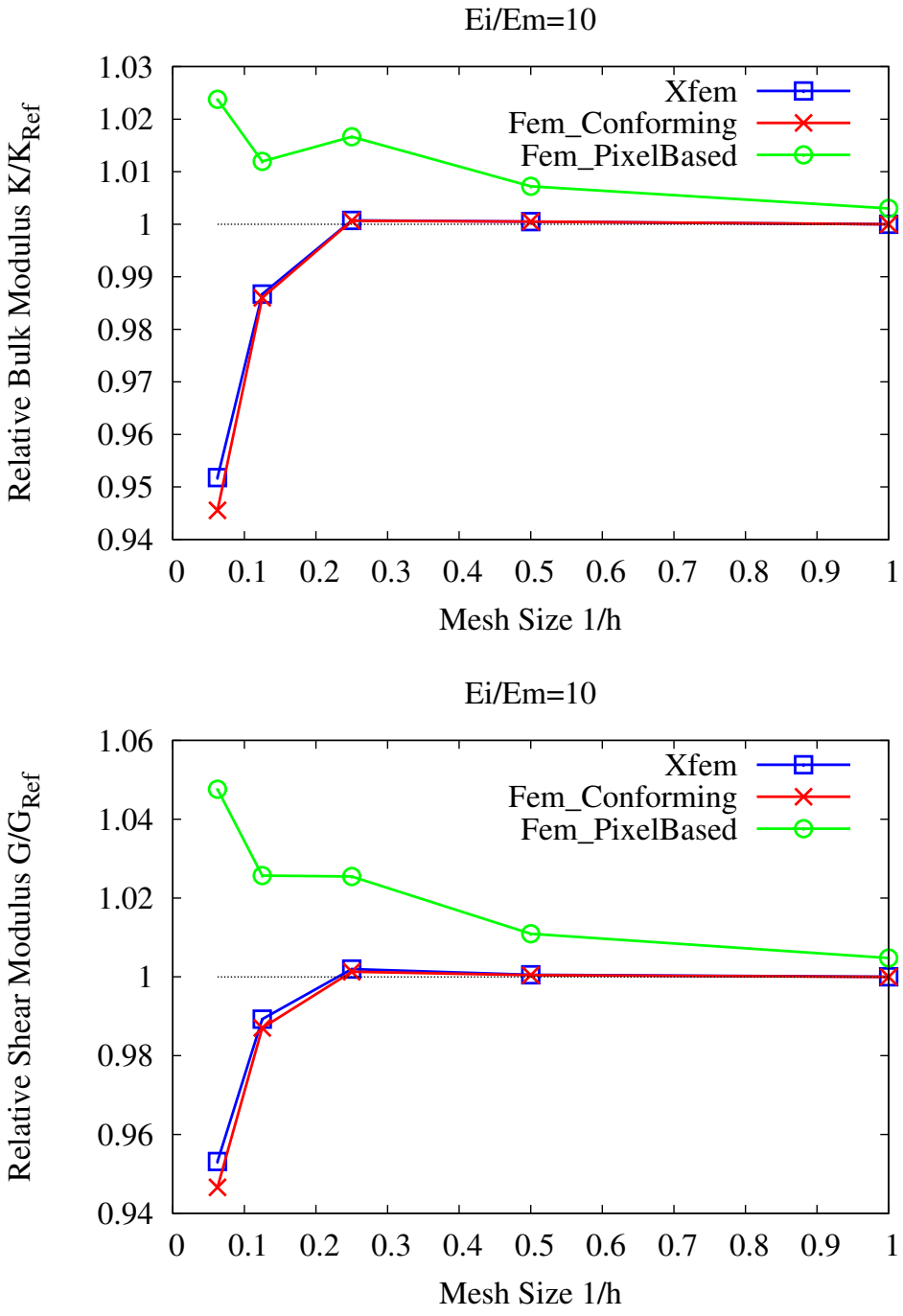

Figure 10: Comparison between voxel-based FEM and X-FEM for macroscopic properties as a function of mesh size h on the contrast $E_i/E_m = 10$

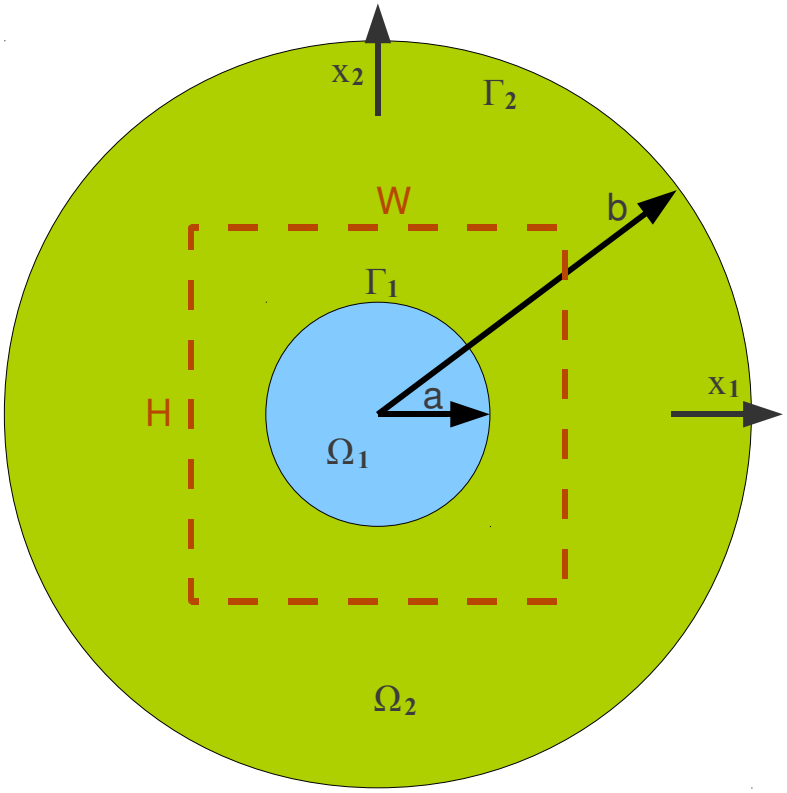

Figure 11: A bimaterial boundary value problem

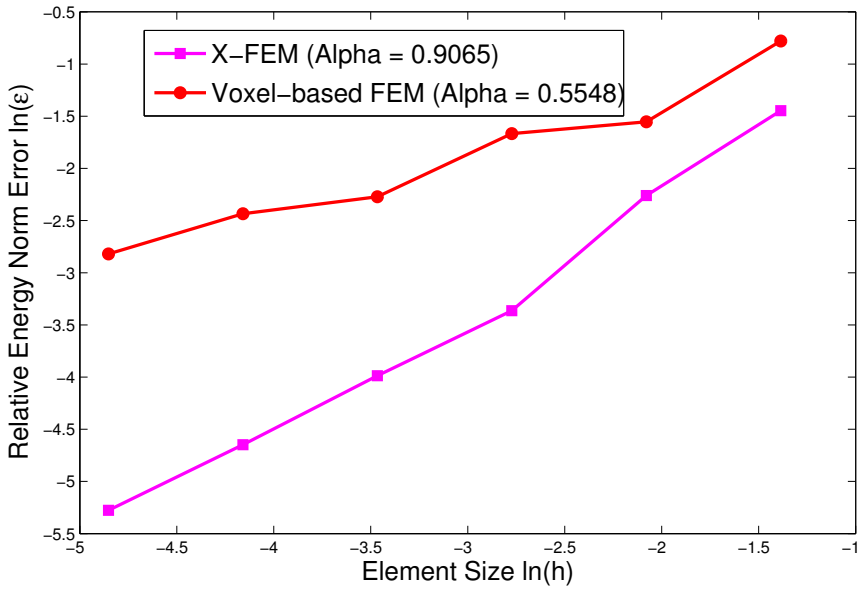

Figure 12: Rates of convergence in energy.

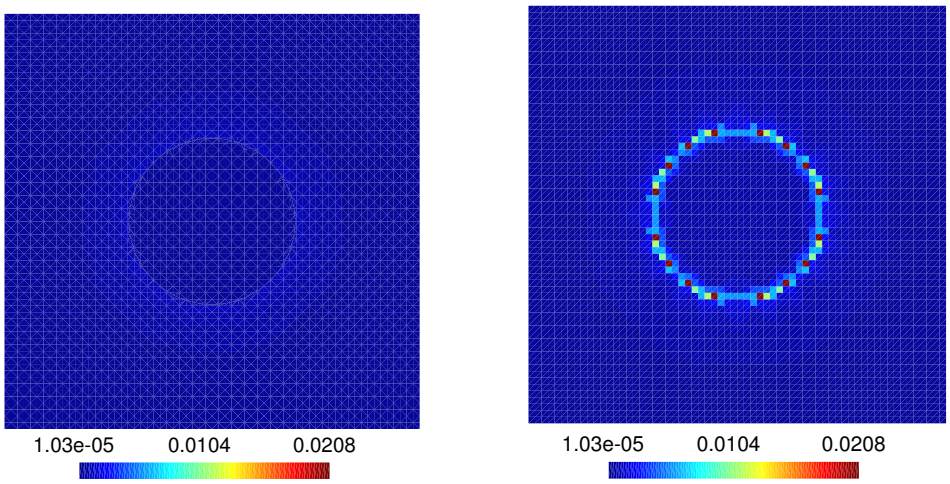

(a) X-FEM (b) Voxel-based FEM

Figure 13: The comparison of the exact local error distribution

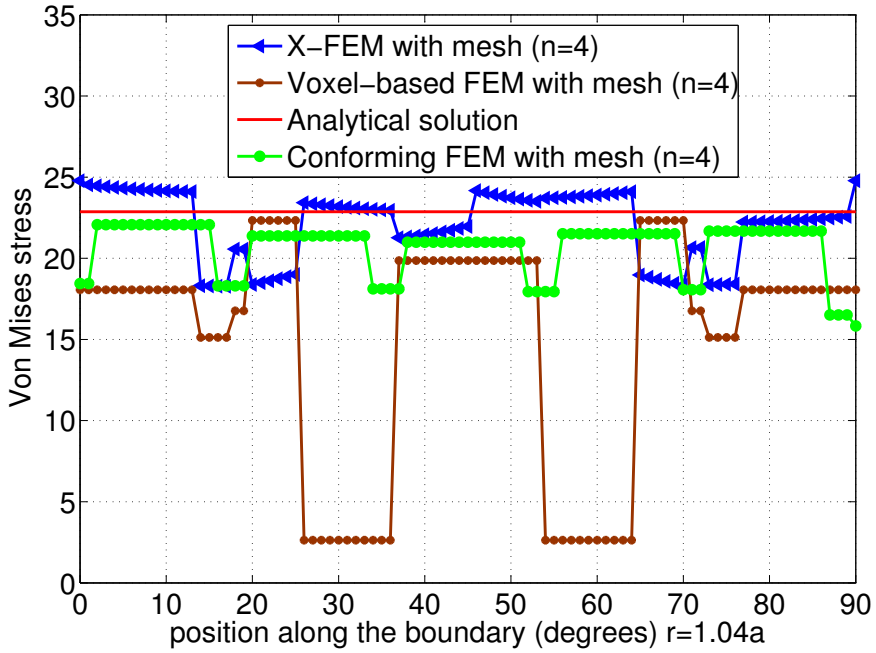

(a) mesh $n = 4$

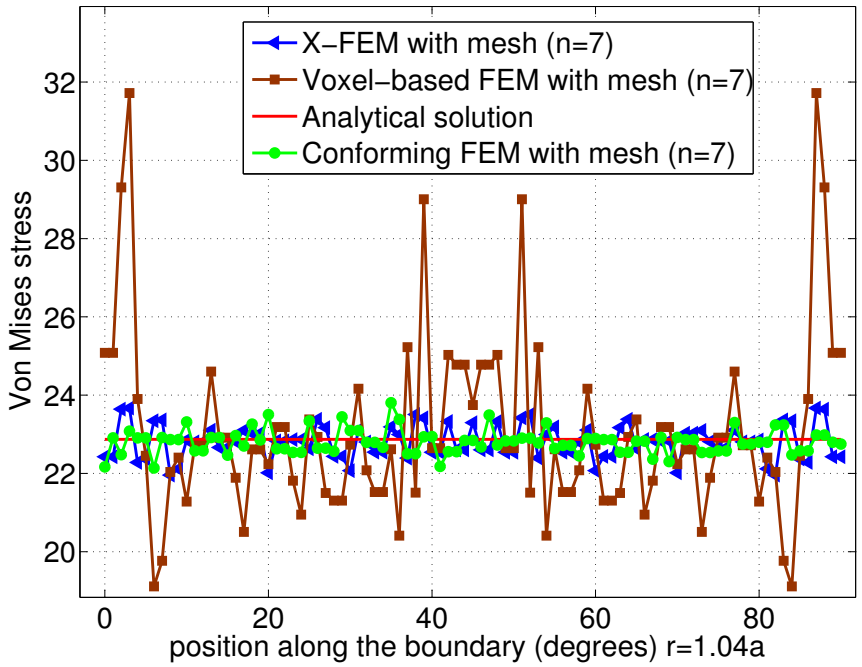

(b) mesh $n = 7$

Figure 14: The Von Mises stress near the boundary interface

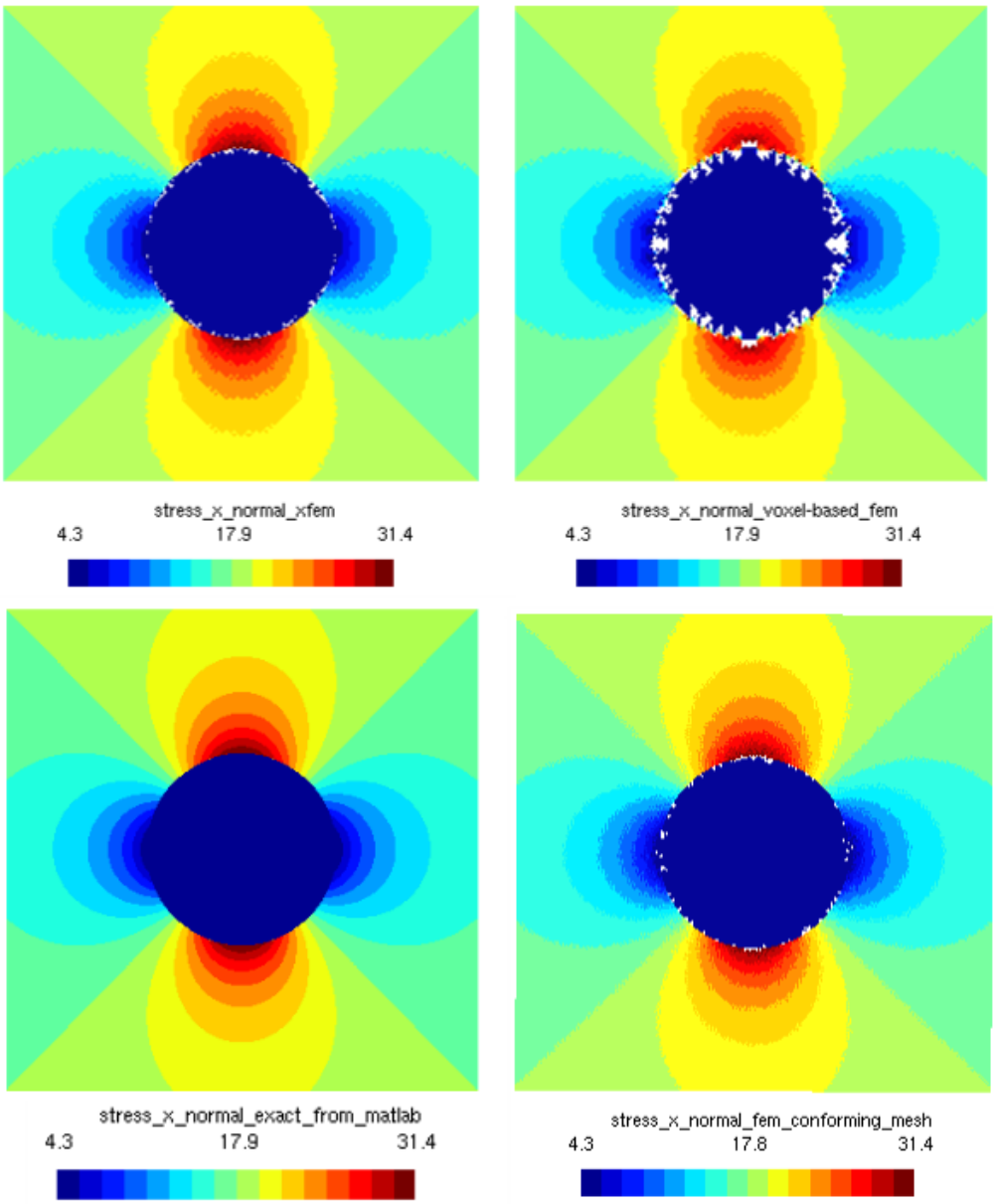

Figure 15: The stress component σ_{11} (left to right, top to bottom: X-FEM, Voxel-based FEM, Exact, FEM conforming). The minimum and maximum value corresponding to each figure is set to that of the exact solution, i.e. $4.3 \sim 31.4$. Consequently, some elements with the values out of this range will be hidden.

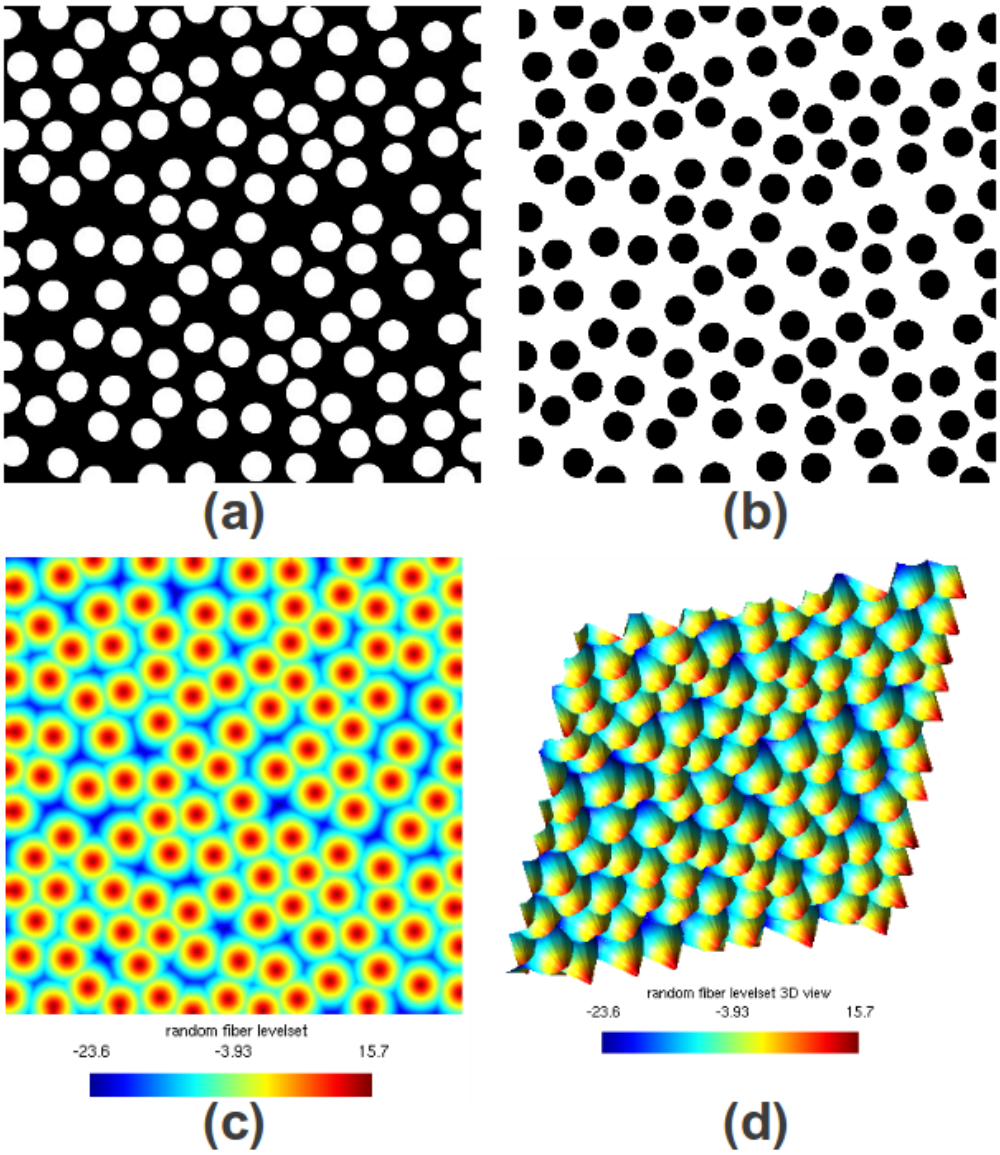

Figure 16: (a) A matrix-fiber composite with randomly-distributed fibers (b) multi-labeled image as the geometry of voxel-based FEM (c) levelset value image (2D view) as the geometry of X-FEM (d) levelset value image (3D view)

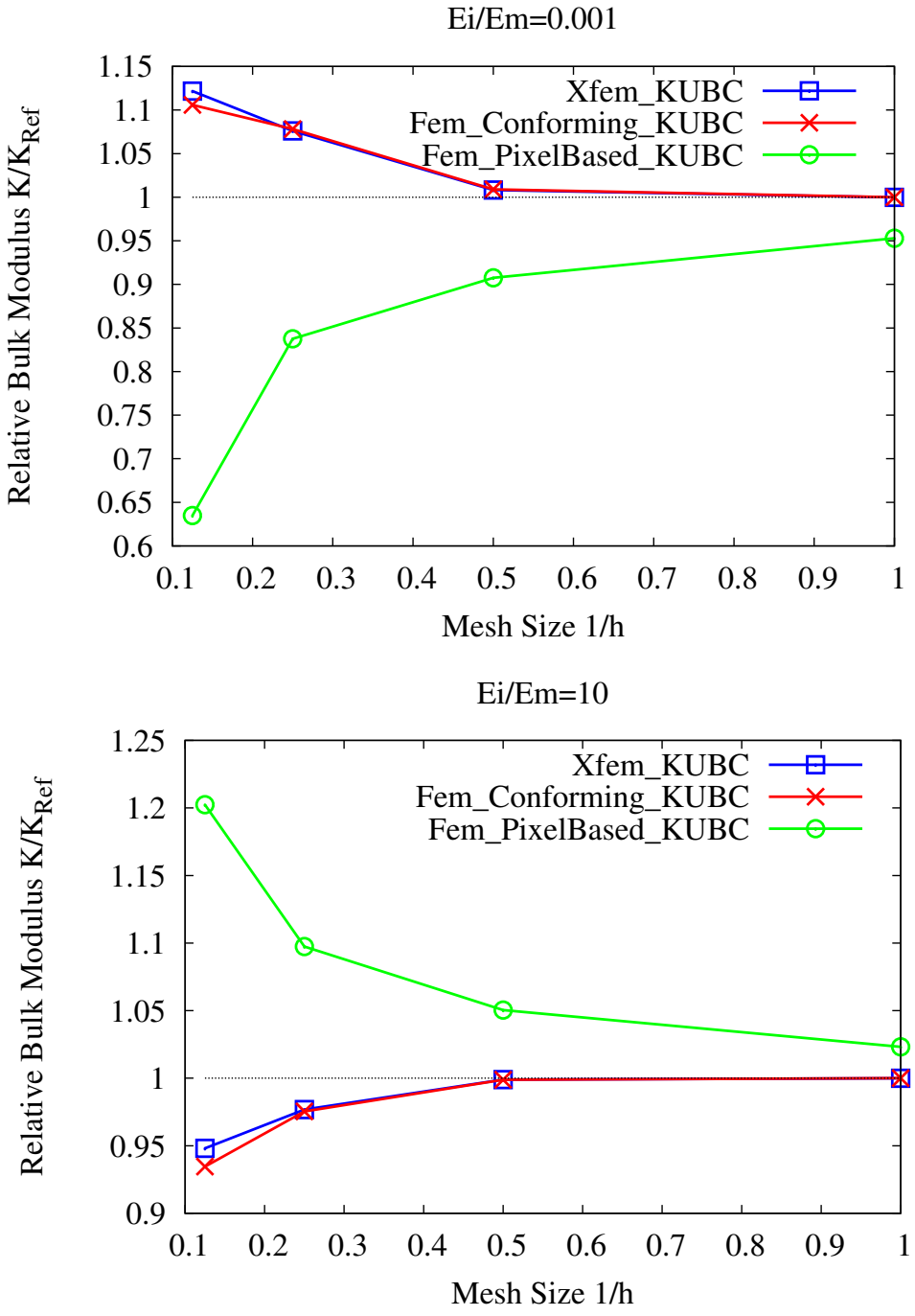

Figure 17: Comparison between voxel-based FEM and X-FEM for bulk modulus as a function of mesh size

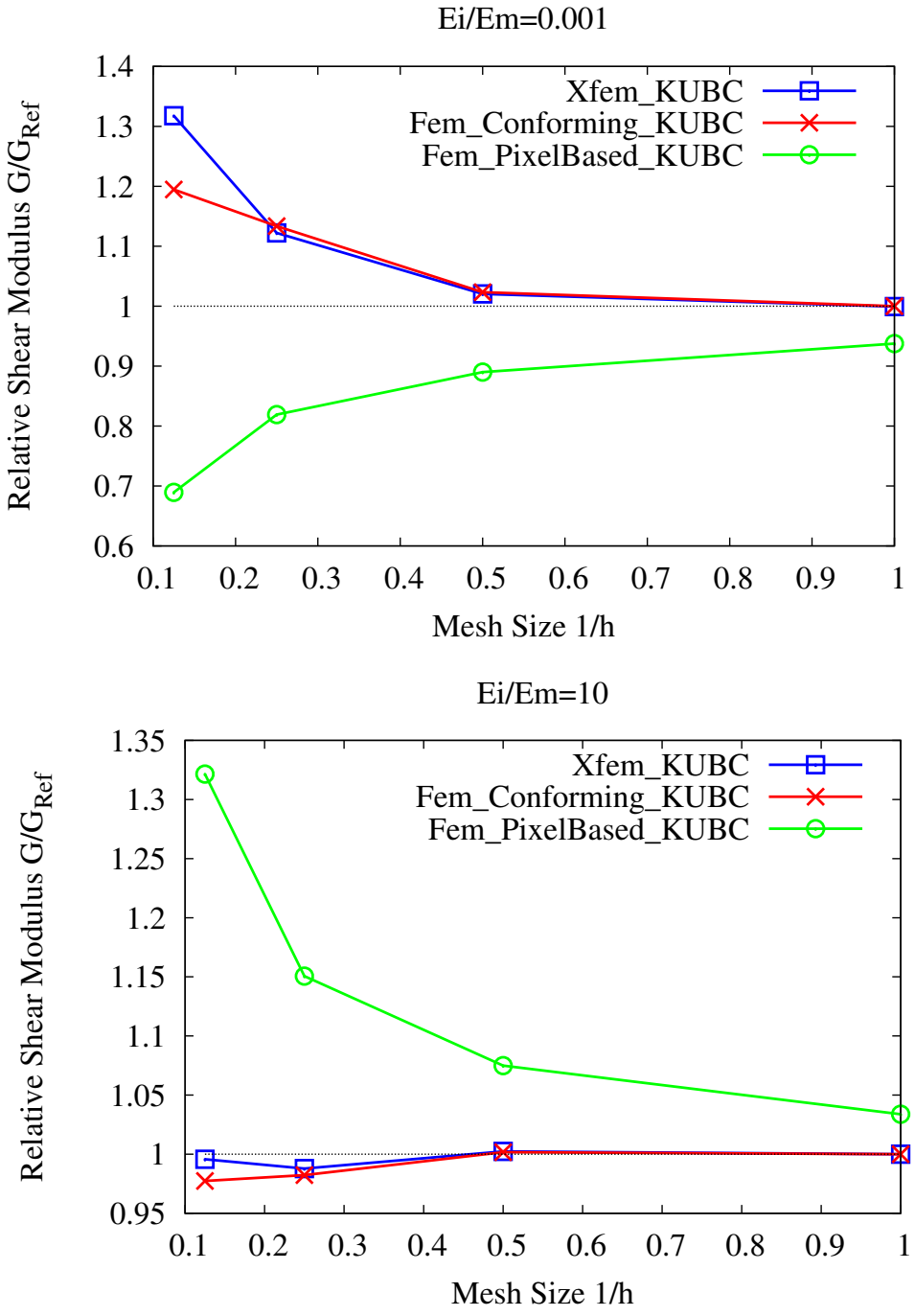

Figure 18: Comparison between voxel-based FEM and X-FEM for shear modulus as a function of mesh size

5.2 A ceramic-metallic composite material

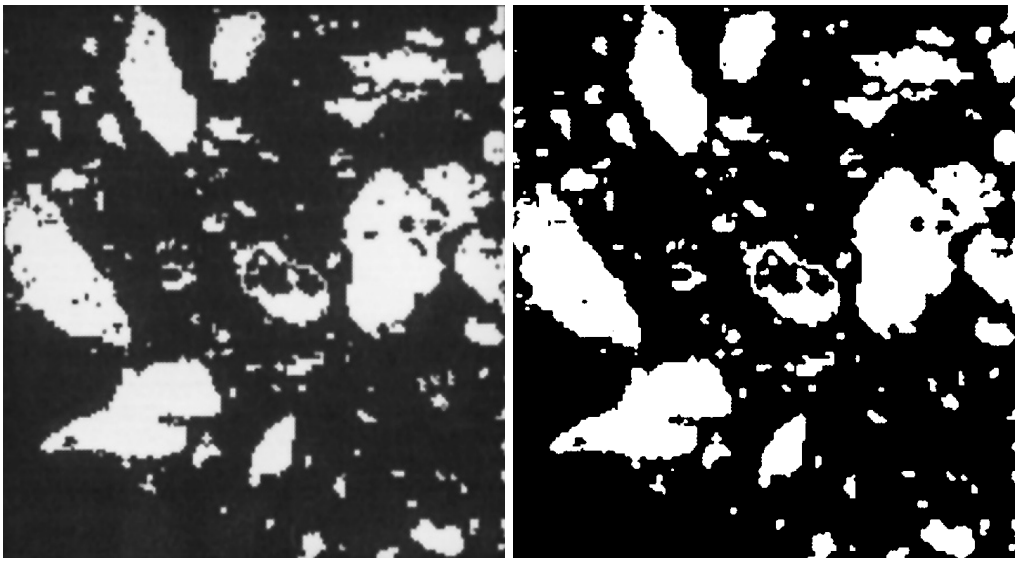

Figure 19: A ceramic-metallic composite 716X790 pixels (left) and the segmented image (right)

A sample of a ceramic-metallic composite 24% TiC-Stellite reported in [13] is also considered in this study as shown in Fig. 19 (image resolution $W = 716$, $H = 790$). The material properties of the two isotropic phases are taken as $E_s = 183\,\text{GPa}$, $\nu_s = 0.3$ (Young's modulus and Poisson's ratio of the phase *stellite*) and $E_t = 447\,\text{GPa}$, $\nu_t = 0.19$ (phase TiC). Since the material studied here can not be considered as a periodic medium, KUBC are imposed on the sample. X-FEM and voxel-based FEM are employed to solve the boundary value problem under plane stress assumption in order to consistent with the numerical simulation reported in [13]. For this composite, since the heterogeneities of the microstructure are clustered in some regions, the octree mesh in Fig. 20 is used in this example. To demonstrate the accuracy of octree mesh solution, four meshes are studied: uniform voxel-based mesh, uniform X-FEM mesh, octree voxel-based mesh, octree X-FEM mesh. For uniform meshes, element size is set to $h = W/2^n$, $n = 6, 7, 8, 9, 10$. For octree mesh, the finest level (near the material interface) has the same element size as uniform mesh, while the mesh is coarser as one moves away from the material interface, see e.g. Fig. 20.

The homogenization computations are carried out on the same RVE as adopted in [13]. The reported effective Young's modulus is approximately 226 GPa in literature. The resulting apparent Young's moduli in this study for different mesh sizes are shown in Tab. 2 and in Fig. 21. It is shown that the two methods provide the effective Young modulus of the reference. With the use of octree mesh, one can significantly decrease the number of degrees of freedom (see Tab. 3), and thus leading to a low computational cost. The relative error of apparent Young's modulus between the uniform mesh and octree mesh is actually about 1%, as shown in Fig. 21. Due to extra degrees of freedom

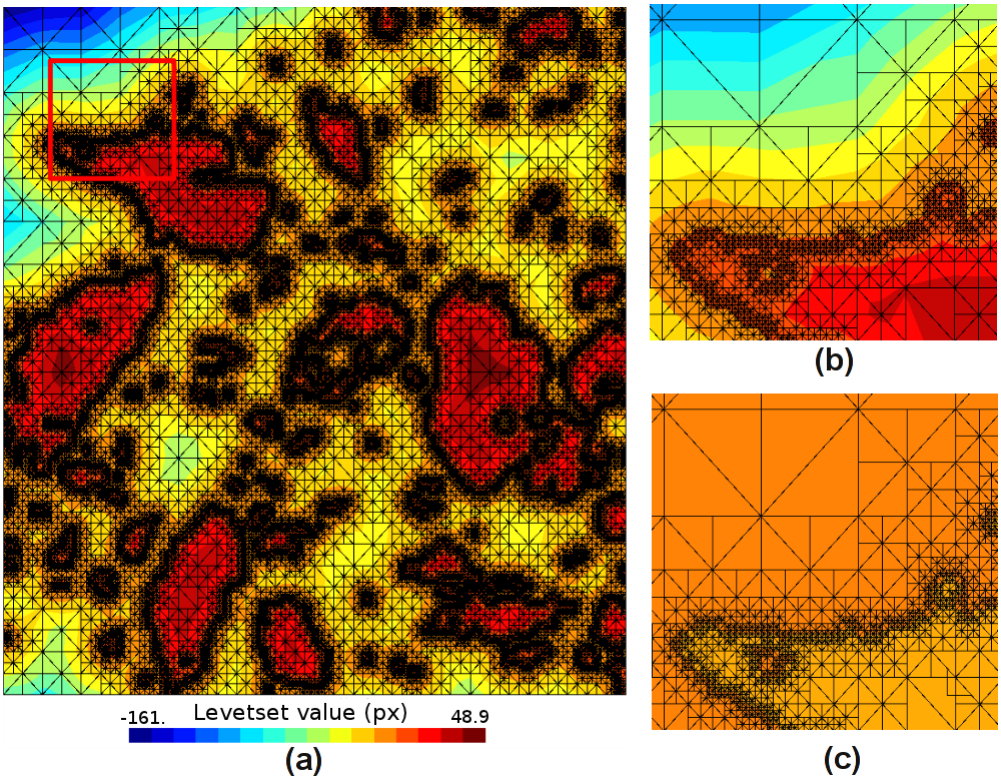

Figure 20: (a) X-FEM octree adaptive mesh (b) Zoomed X-FEM octree adaptive mesh (c) Voxel-based octree adaptive mesh

at enriched nodes for X-FEM, it will lead to a slightly higher computational cost than voxel-based mesh for a fixed mesh density. However, X-FEM usually requires a coarse mesh density than voxel-based FEM for a given accuracy, see Fig. 9 or Fig. 17.

n	6	7	8	9	10
Young	226.09	227.08	227.22	227.16	227.15
Poisson	0.2767	0.2773	0.2779	0.2783	0.2784

(a) X-FEM

n	6	7	8	9	10
Young	226.44	227.89	228.01	227.57	227.39
Poisson	0.2751	0.2757	0.2768	0.2776	0.2780

(b) Voxel-based FEM

Table 2: Apparent Young's modulus (GPa) and Poisson's ratio of Tic/Stellite for different mesh densities where element size $h = W/2^n$.

$h = W/2^n$	uniform	octree	saved (%)
n=6	11110	10300	7.29
n=7	39896	28880	27.61
n=8	147202	70332	52.22
n=9	558120	159018	71.51
n=10	2165942	340296	84.29

(a) X-FEM

$h = W/2^n$	uniform	octree	saved (%)
n=6	7938	7128	10.20
n=7	32258	21242	34.15
n=8	130050	53184	59.10
n=9	522242	123144	76.42
n=10	2093058	267416	87.22

(b) Voxel-based FEM

Table 3: Comparison of costed degree of freedoms

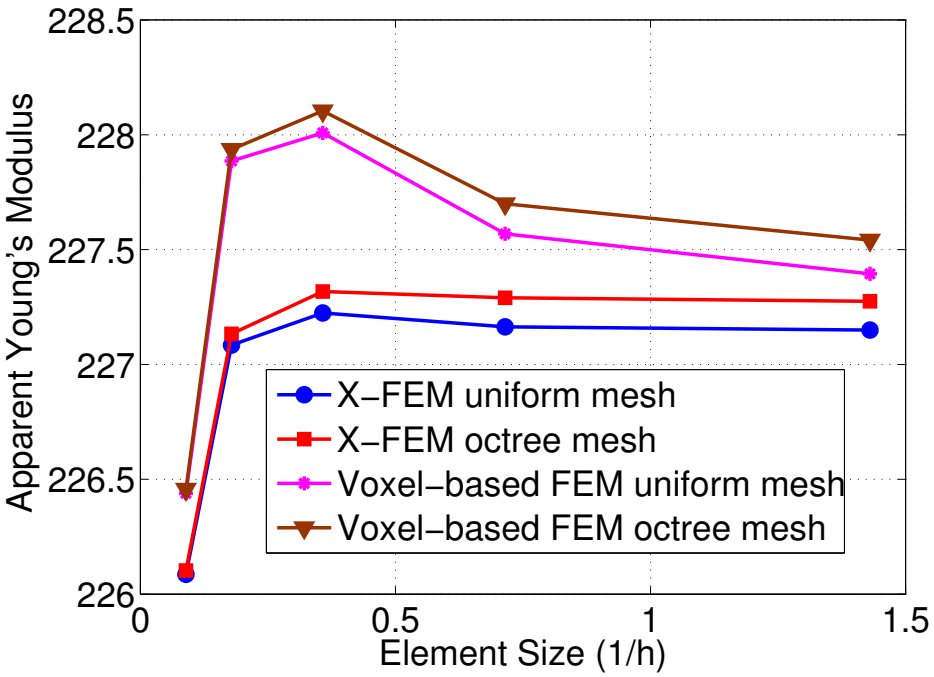

Figure 21: Apparent Young's modulus of Tic/Stellite

5.3 A real 3D foam material

In order to show the capabilities of the X-FEM/levelset approach in 3D, a real foam material is now considered. The material microstructure is shown in Fig. 22, the size of the image being $128 \times 256 \times 256$. This image was obtained from a sample of a cereal solid food [14]. The material is constituted with a void phase and an elastic phase, the constants of the latter being taken as $E_m = 5.8\,\text{GPa}$, $\nu_m = 0.35$. The octree meshing strategy as shown in Fig. 23 (the 1/16 part of the whole model) is used in this example to decrease the computational cost, but still preserving an accurate geometrical representation. In this section we will focus on the comparison between the voxel-based FEM and X-FEM/levelset approach for micro quantities corresponding to the localization problem with KUBC approach.

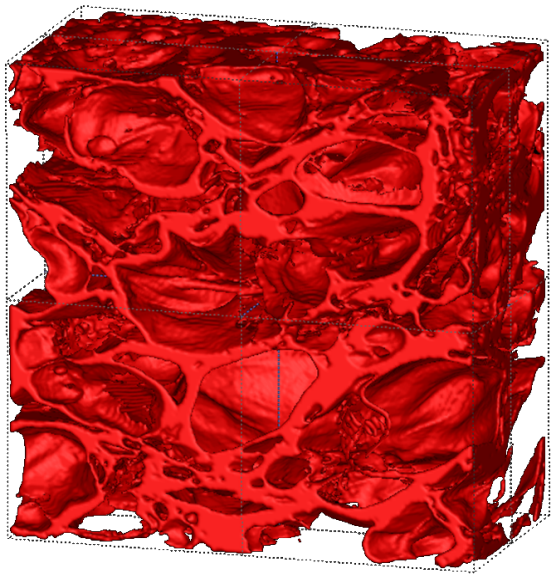

Figure 22: A real foam material

5.3.1 Voxel-based model

In this 3D example, the image has been segmented using the levelset approach presented in Section 2.1. Thus we have a convenient strategy to directly build the voxel-based mesh from the X-FEM mesh. The levelset value is known at each node of X-FEM mesh, accordingly each element can be identified by the following two cases: (i) all the nodal levelset values are positive (resp. negative), the element will be identified as void phase (resp. matrix phase); (ii) positive and negative levelset values co-exist, which indicates that the material interface crosses the element. For case ii, a criterion is introduced to determine whether the element belongs to the matrix phase or not, based on the sign of the levelset value at the element center. If this sign is negative, this element is assigned to the matrix phase. It has been checked that this criterion provides a geometrical

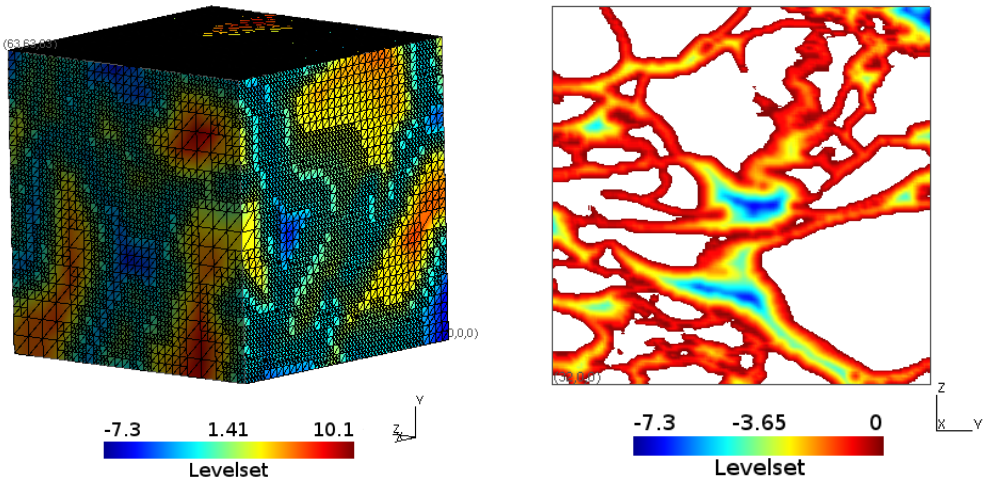

(a) X-FEM octree mesh 64X64X64 (b) One slice of 3D levelset

Figure 23: The octree mesh for 3D model

model with a matrix volume fraction very close to that of the X-FEM mesh (the relative difference is below 1%). As mentioned above, an octree based mesh is used here and the size of the smallest elements corresponds to the voxel size.

5.3.2 Numerical results

The displacements results are analyzed first. In order to highlight microscopic values, the following localization step is performed

$$\boldsymbol{u}_{\text{micro}}(\boldsymbol{x}) = \boldsymbol{u}(x) - \boldsymbol{E} \cdot \boldsymbol{x} \quad \boldsymbol{x} \in \Omega \tag{13}$$

where $\boldsymbol{u}(\boldsymbol{x})$ is the KUBC solution on the RVE. This localization process allows an extraction of microscopic displacement fluctuations. The displacement norm of $\boldsymbol{u}_{\text{micro}}$ is shown in Fig. 24 for a unit macroscopic strain loading. As it follows from Fig. 24a and c, X-FEM holds smooth interfaces owing to the piece-wise linear levelset representation despite using non-conforming mesh (e.g. structured or octree-based). Voxel-based models exhibit jagged interfaces as shown in Fig. 24b and d. In addition, there exist significant topological discrepancies between the geometrical model and voxel-based model. For instance, some connected region are lost for the voxel-based FEM model, as reported in [39, 25].

Similarly, for the stress comparison in Fig. 25, they bear different stress distributions near material interfaces. For this example, it is hard to evaluate the accuracy. However, from the study in Fig. 15, one observed that for voxel-based FEM the stress is either overestimated or underestimated in some regions near the material interface, and in this simulation, one can notice that X-FEM and voxel-based FEM capture quite different maximum Von-mises stresses, see Tab. 4. Furthermore, distributions of the displacement

field obtained by the two approaches appear quite similar, which was also reported in [41].

Loading (10^{-3})	X-FEM	Voxel-based FEM
$E_{xx} = 1$	62.6	30.5
$E_{yy} = 1$	91.7	47.6
$E_{yz} = 1$	68.5	13.6
$E_{xz} = 1$	73.7	17.3

Table 4: Maximum Von-mises stress (MPa) comparison. For the loading, only one macroscopic strain component is not zero, see the first row.

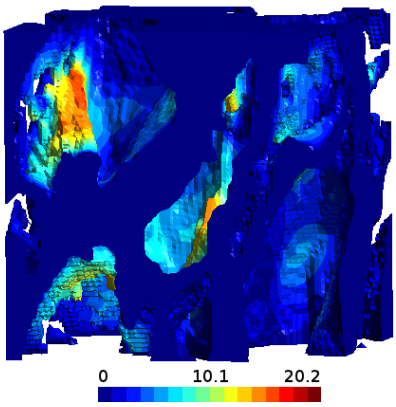

(a) X-FEM

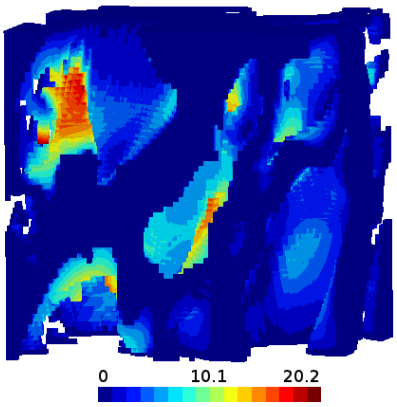

(b) Voxel-based FEM

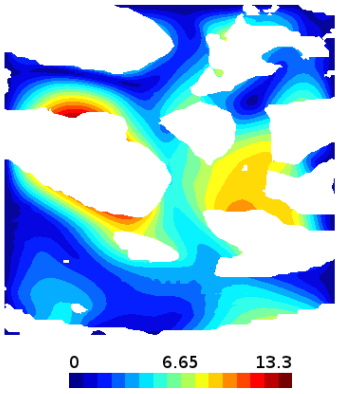

(c) One slice for X-FEM

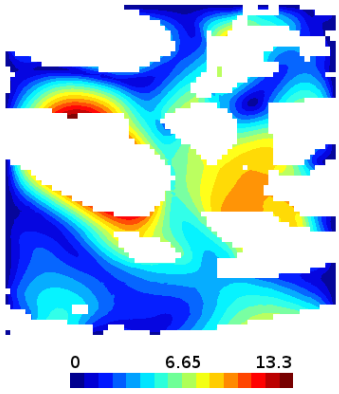

(d) One slice for voxel-based FEM

Figure 24: Displacement fluctuation under uniaxial tension along x axis

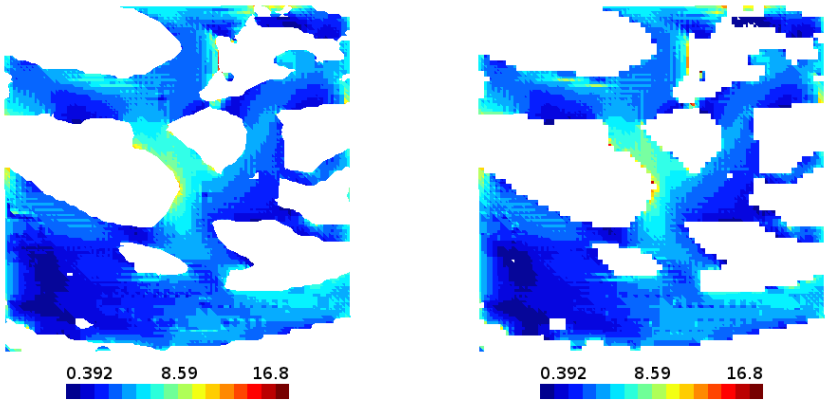

(a) one slice of 3D X-FEM (b) one slice of 3D Voxel-based FEM

Figure 25: Von-mises stress distribution

6 Concluding remarks

This paper aimed to compare the classical voxel-based FEM to the X-FEM/levelset approach developed by the authors [22]. Voxel-based models are widely used mainly because they can be automatically generated from images. This can be done also with the X-FEM/levelset approach, thanks to the X-FEM which allows a non conforming mesh. With voxel based models, the boundary surfaces are jagged, which results from the image digitization. These surfaces can be smoothed, see e.g. [5, 9, 4], but this requires ad-hoc algorithms and hand made operations. By contrast, the X-FEM/levelset model exhibits smoother boundaries from the piece-wise linear representation of the levelset . This means a major difference with the voxel-based model and as it was shown in this paper, it provides to the X-FEM/levelset model a better geometrical accuracy than the voxel-based model. This has several consequences for the solution of homogenization problems, which can be observed at macro and micro scales.

The first one is that any geometrical approximation leads to errors in the volume fraction of material constituents. Consequently this error propagates to the homogenized properties and the use of voxel-based models requires high resolution images in order to control this geometrical error. This error being less important for the X-FEM/levelset model, more accurate results can be obtained starting from an image with a lower resolution than that taken for the voxel-based model. For micro quantities such as the local stresses, the results have shown oscillations and convergence problems for the voxel-based model near the jagged material interface. Better accuracy was obtained with a X-FEM/levelset model, which increases as the mesh is refined. In summary, we have shown through various examples the better numerical efficiency of the X-FEM/levelset approach than the voxel-based FEM.

It has been illustrated for a 2D example that X-FEM/levelset approach is comparable to conforming FEM in terms of micro- and macro-quantities. For the 3D foam example, such comparison has not been performed because it requires a smoothing of the voxel-based geometry. However 3D results given in [29] for a spherical inclusion show that the convergence rate of the X-FEM is very close to the conforming FEM. Due to the enriched dofs, X-FEM bears a higher computational cost than conforming FEM. But the key advantage of the X-FEM is that a structured mesh independent of the geometry can be used. Instead it is challenging and time-consuming to generate a conforming mesh, especially for materials with complex 3D microstructures. Thus, X-FEM exhibits a very good computational efficiency, without any meshing effort.

An octree-based adaptive strategy was considered in numerical examples to keep maximal geometrical accuracy while decreasing the computational cost. However, this strategy was quite crude (and purely geometrical). A straightforward improvement could be obtained by considering the curvature as a criterion for mesh adaptation. Otherwise, the multiple levelset approach proposed by [38] could also be used as a mean to represent accurately complex geometries on coarse meshes. Finally, an alternative strategy has been presented recently. It is based on the use of a high-order approximation whose mesh support is independent of the support of the levelset [8, 23, 24].

Acknowledgments

We would like to gratefully acknowledge the financial support of China Scholarship Council (CSC) for the first author, and of INRA and CNRS through the project PEPS 'SIFRAGRAM'. Thanks also to Dr S. Guessasma for providing us the foam image.

References

[1] Arbenz P, Flaig C (2008) On Smoothing Surfaces in Voxel Based Finite Element Analysis of Trabecular Bone. Lect Notes Comput Sci 4818(1):69

[2] Belytschko T, Black T (1999) Elastic crack growth in finite elements with minimal remeshing. Int J Numer Methods Eng 45(5):601–620

[3] Belytschko T, Parimi C, Moës N, Sukumar N, Usui S (2003) Structured extended finite element methods for solids defined by implicit surfaces. Int J Numer Methods Eng 56(4):609–635

[4] Boyd S, Müller R (2006) Smooth surface meshing for automated finite element model generation from 3D image data. J Biomech 39(7):1287–95

[5] Camacho D, Hopper R, Lin G, Myers B (1997) An improved method for finite element mesh generation of geometrically complex structures with application to the skullbase. J Biomech 30(10):1067–1070

[6] Cebral J, Löhner R (2001) From medical images to anatomically accurate finite element grids. Int J Numer Methods Eng 51(8):985–1008

[7] Charras GT, Guldberg RE (2000) Improving the local solution accuracy of large-scale digital image-based finite element analyses. J Biomech 33(2):255–259

[8] Dréau K, Chevaugeon N, Moës N (2010) Studied X-FEM enrichment to handle material interfaces with higher order finite element. Comput Method Appl M 199(29-32):1922–1936

[9] Frey P (2004) Generation and adaptation of computational surface meshes from discrete anatomical data. Int J Numer Methods Eng 60(6):1049–1074

[10] Frey P, George PL (2000) Mesh generation: application to finite elements. Hermes Science Europe Ltd., UK

[11] Fries TP, Belytschko T (2010) The extended / generalized finite element method : An overview of the method and its applications. Int J Numer Methods Eng 84(3):253–304

[12] Gitman I, Askes H, Sluys L (2007) Representative volume: Existence and size determination. Eng Fract Mech 74(16):2518–2534

[13] Golanski D, Terada K, Kikuchi N (1997) Macro and micro scale modeling of thermal residual stresses in metal matrix composite surface layers by the homogenization method. Comput Mech 19(3):188–202

[14] Guessasma S, Chaunier L, Della Valle G, Lourdin D (2011) Mechanical modelling of cereal solid foods. Trends Food Sci Tech 22(4):142–153

[15] Guldberg RE, Hollister SJ, Charras GT (1998) The accuracy of digital image-based finite element models. J Biomech Eng 120(2):289–95

[16] Hollister SJ, Kikuchi N (1994) Homogenization theory and digital imaging: A basis for studying the mechanics and design principles of bone tissue. Biotechnol Bioeng 43(7):586–96

[17] Ibanez L, Schroeder W, Ng L, Cates J (2005) The ITK Software Guide. Kitware, Inc. ISBN 1-930934-15-7, http://www.itk.org/ItkSoftwareGuide.pdf, 2nd edn

[18] Jiang M, Jasiuk I, Ostoja-Starzewski M (2002) Apparent elastic and elastoplastic behavior of periodic composites. Int J Solids Struct 39(1):199–212

[19] Kanit T, Forest S, Galliet I, Mounoury V, Jeulin D (2003) Determination of the size of the representative volume element for random composites: statistical and numerical approach. Int J Solids Struct 40(13-14):3647–3679

[20] Kanit T, Nguyen F, Forest S, Jeulin D, Reed M, Singleton S (2006) Apparent and effective physical properties of heterogeneous materials: Representativity of samples of two materials from food industry. Comput Method Appl M 195(33-36):3960–3982

[21] Keyak J, Meagher J, Skinner H, Motejr C (1990) Automated three-dimensional finite element modelling of bone: a new method. J Biomed Eng 12(5):389–397

[22] Legrain G, Cartraud P, Perreard I, Moës N (2011) An X-FEM and level set computational approach for image-based modelling: Application to homogenization. Int J Numer Methods Eng 86(7):915–934

[23] Legrain G, Chevaugeon N, Dréau K (2011) High order eXtended Finite Element Method and Level Sets: Uncoupling geometry and approximation. In: ECCOMAS XFEM 2011 Conference, Cardiff

[24] Legrain G, Chevaugeon N, Dréau K (2012) High Order X-FEM and Levelsets for Complex Microstructures: Uncoupling Geometry and Approximation. Submitted to: Comput Method Appl M

[25] Maire E, Fazekas A, Salvo L, Dendievel R, Youssef S, Cloetens P, Letang J (2003) X-ray tomography applied to the characterization of cellular materials. Related finite element modeling problems. Compos Sci Technol 63(16):2431–2443

[26] Melenk J, Babuška I (1996) The partition of unity finite element method: basic theory and applications. Comput Method Appl M 139(1-4):289–314

[27] Michel J, Moulinec H, Suquet P (1999) Effective properties of composite materials with periodic microstructure: a computational approach. Comput Method Appl M 172(1-4):109–143

[28] Mishnaevsky L (2005) Automatic voxel-based generation of 3D microstructural FE models and its application to the damage analysis of composites. Mat Sci Eng A-Struct 407(1-2):11–23

[29] Moës N, Cloirec M, Cartraud P, Remacle J (2003) A computational approach to handle complex microstructure geometries. Comput Method Appl M 192(28-30):3163–3177

[30] Osher S, Sethian J (1988) Fronts propagations with curvature dependent speed: Algorithms based on Hamilton-Jacobi formulations. Journal of Computational Physics 79:12–49

[31] Ostoja-Starzewski M (2008) Microstructural randomness and scaling in mechanics of materials. Chapman and Hall/CRC, Florida

[32] Sakellariou A, Arns C, Sheppard A, Sok R, Averdunk H, Limaye A, Jones A, Senden T, Knackstedt M (2007) Developing a virtual materials laboratory. Mater Today 10(12):44–51

[33] Sethian J (1999) Level Set Methods and Fast Marching Methods Evolving Interfaces in Computational Geometry, Fluid Mechanics, Computer Vision, and Materials Science 2nd Edition

[34] Still M (2006) The Definitive Guide to ImageMagick – Learn how to use the open source ImageMagick program to transform images, 1st edn. Apress

[35] Stolarska M, Chopp DL, Moës N, Belytschko T (2001) Modelling Crack Growth by Level Sets and the Extended Finite Element Method. International Journal for Numerical Methods in Engineering 51(8):943–960, URL mypapers/stola.pdf

[36] Sukumar N, Chopp D, Moës N, T (2001) Modeling holes and inclusions by level sets in the extended finite-element method. Comput Method Appl M 190(46-47):6183–6200

[37] Terada K, Miura T, Kikuchi N (1997) Digital image-based modeling applied to the homogenization analysis of composite materials. Comput Mech 20:331–346

[38] Tran AB, Yvonnet J, He QC, Toulemonde C, Sanahuja J (2011) A multiple level set approach to prevent numerical artefacts in complex microstructures with nearby inclusions within XFEM. Int J Numer Methods Eng 85(11):1436–1459

[39] Ulrich D, van Rietbergen B, Weinans H, Rüegsegger P (1998) Finite element analysis of trabecular bone structure: a comparison of image-based meshing techniques. J Biomech 31(12):1187–92

[40] Vese L, Chan T (2002) A multiphase level set framework for image segmentation using the Mumford and Shah model. Int J Comput Vision 50(3):271–293

[41] Viceconti M, Bellingeri L, Cristofolini L, Toni A (1998) A comparative study on different methods of automatic mesh generation of human femurs. Med Eng Phys 20(1):1–10

[42] Wang ZL, Teo JCM, Chui CK, Ong SH, Yan CH, Wang SC, Wong HK, Teoh SH (2005) Computational biomechanical modelling of the lumbar spine using marching-cubes surface smoothened finite element voxel meshing. Comput Methods Programs Biomed 80(1):25–35

[43] Young PG, Beresford-West TBH, Coward SRL, Notarberardino B, Walker B, Abdul-Aziz A (2008) An efficient approach to converting three-dimensional image data into highly accurate computational models. Philos Transact A Math Phys Eng Sci 366(1878):3155–73

[44] Yvonnet J, He QC, Toulemonde C (2008) Numerical modelling of the effective conductivities of composites with arbitrarily shaped inclusions and highly conducting interface. Compos Sci Technol 68(13):2818–2825

[45] Yvonnet J, Quang H, He Q (2008) An xfem/level set approach to modelling surface/interface effects and to computing the size-dependent effective properties of nanocomposites. Comput Mech 42:119–131